



# Free vibration analysis of functionally graded carbon nanotube-reinforced composite plates using the element-free $kp$ -Ritz method in thermal environment



Z.X. Lei <sup>a,b,c</sup>, K.M. Liew <sup>b,c,\*</sup>, J.L. Yu <sup>a,c</sup>

<sup>a</sup> CAS Key Laboratory of Mechanical Behavior and Design of Materials, University of Science and Technology of China, PR China

<sup>b</sup> Department of Civil and Architectural Engineering, City University of Hong Kong, Kowloon, Hong Kong

<sup>c</sup> USTC-CityU Joint Advanced Research Centre, Suzhou, Jiangsu, PR China

## ARTICLE INFO

### Article history:

Available online 14 June 2013

### Keywords:

Free vibration  
Carbon nanotube  
Composite  
First order shear deformation theory  
Mesh-free method

## ABSTRACT

In this paper, a free vibration analysis of functionally graded nanocomposite plates reinforced by single-walled carbon nanotubes (SWCNTs), using the element-free  $kp$ -Ritz method, is presented. Different types of distributions of uniaxially aligned SWCNTs are considered. The material properties of functionally graded carbon nanotube-reinforced composites (FG-CNTRCs) are assumed to be graded through the thickness direction according to several linear distributions of the volume fraction of carbon nanotubes. The governing equations are based on the first-order shear deformation plate theory and the two-dimensional displacement fields are approximated by mesh-free kernel particle functions. Convergence and comparison studies have been carried out to verify the stability and accuracy of the present method for analysis of free vibration of various types of CNTRC plates. In computational simulation, several examples are presented to analyze the effects of carbon nanotube volume fraction, plate width-to-thickness ratio, plate aspect ratio and temperature change on natural frequencies and mode shapes of various types of FG-CNTRC plates, and results for uniformly distributed (UD) CNTRC plates are also provided for comparison. The effect of boundary conditions is also examined.

© 2013 Elsevier Ltd. All rights reserved.

## 1. Introduction

Carbon nanotubes (CNTs), a new advanced material of high strength and stiffness with high aspect ratio and low density, have attracted much attention of researchers. Many experimental and theoretical investigations indicated that CNTs have extraordinary high stiffness-to-weight and strength-to-weight ratio properties. Treacy et al. [1] found that CNTs have exceptionally high Young's moduli in the terapascal (TPa) range. Wong et al. [2] discovered that multi-walled CNTs were about two times as stiff as the silicon carbide nanorods using atomic force microscopy. Salvetat et al. [3] reported that the elastic and shear moduli of individual single-walled nanotubes ropes were in the order of 1 TPa and 1 GPa. Based on a first-principles cluster method within the framework of local density approximation, Zhou et al. [4] examined the morphology, mechanical properties and electronic structure of single-walled carbon nanotubes (SWCNTs). The reported exceptional properties of nanotubes have motivated researchers to investigate experimentally of nanotube-based composites. Jin et al. [5] re-

ported a method to fabricate polymer-based composites with aligned carbon nanotubes where the orientation and the degree of alignment were determined by X-ray diffraction. Bower et al. [6] fabricated and investigated polymer composites reinforced by uniaxially oriented multi-walled carbon nanotubes by transmission electron microscopy. By using a combination of solvent casting and melt mixing method, Haggemueller and co-workers [7] dispersed aligned SWCNT in poly (methyl methacrylate) (PMMA). Thostenson and Chou [8] investigated a scalable calendaring approach for achieving dispersion of CVD-grown multi-walled carbon nanotubes through intense shear mixing.

Motivated by their remarkable mechanical properties, carbon nanotubes (CNTs) have potential for being used for reinforcement of high strength and light-weight polymer composites. Many researchers have paid much attention to the CNT-reinforced composites [9–11]. Ajayan et al. [12] first studied composites reinforced by aligned CNT arrays and discovered that the reinforced composites had excellent mechanical properties. Morphological and mechanical properties of semicrystalline and amorphous polymer composites reinforced by multi-walled CNTs were investigated by Cadek et al. [13]. They found that the presence of nanotubes nucleates crystallization of the polymer and this crystal growth enhanced matrix-nanotube stress transfer. Since the

\* Corresponding author at: Department of Civil and Architectural Engineering, City University of Hong Kong, Kowloon, Hong Kong.

E-mail address: [kmliew@cityu.edu.hk](mailto:kmliew@cityu.edu.hk) (K.M. Liew).

interaction at the polymer and nanotube interface is highly dependent on the local molecular structure and bonding, a constitutive model has been proposed for carbon nanotube reinforced composites (CNTRCs) by using an equivalent-continuum modeling method [14]. Griebel and Hamaekers [15] examined the elastic moduli of CNTRCs using molecular dynamic simulations and found the results were in excellent agreement with solutions obtained by the macroscopic rule of mixtures. Fidelus et al. [16] studied thermo-mechanical properties of epoxy based nanocomposites with low weight fractions of randomly oriented single- and multi-walled CNTs. Although studies of mechanical, electrical and thermal properties of nanocomposites are quite useful, the ultimate purpose of development of this advanced material is to explore potential applications of CNTRCs in actual structures, such as CNT-reinforced beams, plates or shells. Wuite and Adali [17] analyzed symmetric cross-ply and angle-ply laminated beams stacked with multiple transversely isotropic layers reinforced by CNTs in differently aligned directions and isotropic beams. Analyses of pure bending and bending-induced buckling of a nanocomposite beam based on a continuum mechanical model were reported by Vodenitcharova and Zhang [18]. The results demonstrated that in the thicker matrix layers single-walled CNT buckled at smaller bending angles and greater flattening ratios. By employing an equivalent continuum model (the Mori–Tanaka scheme), Formica et al. [19] studied vibration behaviors of cantilevered CNTRC plates. Based on the classical laminated plate theory and third-order shear deformation theory, Arani et al. [20] analytically and numerically investigated buckling behaviors of laminated composite plates in which optimal orientations of CNTs required to achieve the highest critical load and the corresponding modes shape were calculated for different kinds of boundary conditions, as well as aspect ratios of the plates.

Functionally graded materials (FGMs) are a new breed of composite materials with properties that vary spatially according to a certain non-uniform distribution of the reinforcement phase. Much work has been done on FGMs in a wide range of fields since the concept of FGMs was first proposed in 1984 [21,22]. Stimulated by the concept of FGMs, CNT-based composite plates were proposed by Shen [23]; nonlinear bending analysis of functionally graded carbon nanotube-reinforced composite (FG-CNTRC) plates in thermal environments was studied. By using the finite element method (FEM), bending and free vibration analyses were carried out for various types of FG-CNTRC plates in [24]. Ke et al. [25] presented a nonlinear free vibration analysis of FG-CNTRC beams based on the Timoshenko beam theory. They found that both linear and nonlinear frequencies of FG-CNTRC beam with symmetrical distribution of CNTs were higher than those of beams with uniform or asymmetrically distributed CNTs. Then Shen and Zhang [26] reported thermal buckling and postbuckling behaviors of FG-CNTRC plates which were subjected to in-plane temperature variation.

In recent years, mesh-free methods have attracted attention of many researchers. Compared to FEMs, mesh-free methods can eliminate mesh distortion due to large deformation and avoid the need for remeshing, which is time-consuming and computationally intensive. The first mesh-free method, called smoothed particle hydrodynamics (SPH), was developed and used by Lucy for modeling astrophysical phenomena without boundaries [27]. Based on NURBS (Non-Uniform Rational B-Splines), Hughes et al. [28] reported an isogeometric analysis to construct an exact geometric model. Nayroles et al. [29] presented a diffuse approximation method by using the moving least squares approximations in the Galerkin method. Arroyo and Ortiz [30] reported local maximum-entropy approximation schemes which can be considered as a convenient basis for the numerical solution of partial differential equations in the style of mesh-free Galerkin methods. Then Cyron et al. [31] extended these schemes to second-order maximum-entropy approximation schemes. With combination of concepts from opti-

mal transportation theory with material-point sampling and maximum-entropy mesh-free interpolation, Li et al. [32] developed an optimal transportation mesh-free method for simulating general solid and fluid flows, including fluid–structure interaction. Based on the local maximum entropy approach, Fraternali et al. [33] presented a mesh-free method for the curvature estimation of membrane networks. Belytschko et al. [34] refined and modified the diffuse element method to simulate the static and dynamic crack problems which is called the element free Galerkin method. Krysl and Belytschko applied the element-free Galerkin method for analyses of thin plates and shells [35,36] and Liew et al. employed it to analyze the pseudoelastic behavior of a SMA beam [37] and buckling behaviors of corrugated plates [38]. Through the FSDT mesh-free method, Peng et al. [39] presented a free vibration analysis of fold plates. Zhu and Liew [40] reported a free vibration analysis of moderately thick functionally graded plates by local Kriging meshless method. Other advanced mesh-free methods including the reproducing kernel particle method and the meshless local Petrov–Galerkin method have also been successfully used in a variety of engineering problems [41–43].

This paper presents a free vibration analysis of various types of CNTRC plates with arbitrary boundary conditions using the element-free  $kp$ -Ritz method, which has already been successfully applied for many problems [44–47]. The single-walled carbon nanotubes (SWCNTs) are assumed to be uniformly distributed or functionally graded along the thickness direction of plates and the effective material properties of CNTRCs can be estimated by either the Eshelby–Mori–Tanaka approach or the extended rule of mixture. The first-order shear deformation plate theory is used to account for transverse shear deformation and rotary inertia. Convergence and comparison studies are provided to verify the stability and accuracy of the proposed method for free vibration analysis of CNTRC plates. The effects of boundary condition, CNT volume fraction, plate width-to-thickness ratio, plate aspect ratio and temperature change on characteristics of the frequency are also examined in detail.

## 2. Functionally graded CNTRC plates

Four types of distributions of CNTs in CNTRC plates with length  $a$ , width  $b$  and thickness  $h$  are considered in this paper, as shown in Fig. 1. UD represents the uniform distribution and the other three types of functionally graded distributions of CNTs are denoted by FG-V, FG-O and FG-X. For the type of FG-V, the top surface of the CNTRC plate is CNT-rich. In FG-X, the mid-plane of the CNTRC plate is CNT-rich and in case of FG-O, both top and bottom surfaces of the CNTRC plate are CNT-rich. Distributions of CNTs along the thickness direction of these four types of CNTRC plates are assumed to be as

$$V_{CNT}(z) = \begin{cases} V_{CNT}^* & \text{(UD CNTRC)} \\ (1 + \frac{2z}{h})V_{CNT}^* & \text{(FG - V CNTRC)} \\ 2\left(1 - \frac{2|z|}{h}\right)V_{CNT}^* & \text{(FG - O CNTRC)} \\ 2\left(\frac{2|z|}{h}\right)V_{CNT}^* & \text{(FG - X CNTRC)} \end{cases}, \quad (1)$$

where

$$V_{CNT}^* = \frac{w_{CNT}}{w_{CNT} + (\rho^{CNT}/\rho^m) - (\rho^{CNT}/\rho^m)w_{CNT}}, \quad (2)$$

where  $w_{CNT}$  is the fraction of mass of the CNTs, and  $\rho^m$  and  $\rho^{CNT}$  are densities of the matrix and CNTs, respectively. The CNT volume fraction of UD-CNTRC plate and other three types FG-CNTRC plates are assumed to be  $V_{CNT} = V_{CNT}^*$ , that means UD-CNTRC plate and the other three types FG-CNTRC plates have the same mass volume of CNTs.

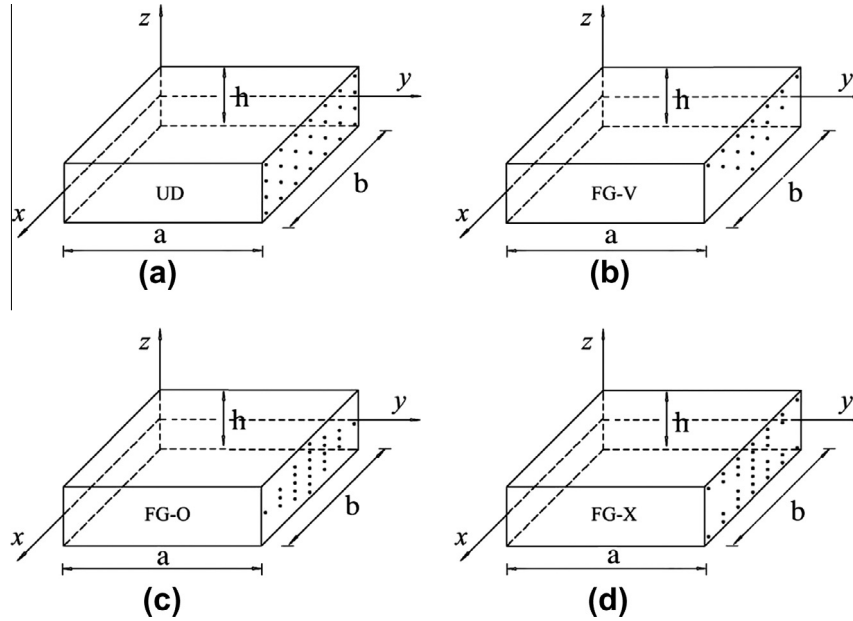


Fig. 1. Configurations of carbon nanotube reinforced composite plates. (a) UD CNTRC plate; (b) FG-V CNTRC plate; (c) FG-O CNTRC plate; and (d) FG-X CNTRC plate.

Several micromechanical models have been successfully developed to predict the effective material properties of CNT-reinforced nanocomposites such as Eshelby–Mori–Tanaka scheme [19,48,49] and the extended rule of mixture [23,26,50]. A comparison study of Eshelby–Mori–Tanaka scheme and the extended rule of mixture is also conducted for the vibration analysis of continuously graded carbon nanotubes-reinforced cylindrical panels in [48].

### 2.1. Extended rule of mixture

According to the extended rule of mixture, effective material properties of CNTRC plates can be expressed as [23]

$$E_{11} = \eta_1 V_{CNT} E_{11}^{CNT} + V_m E^m, \quad (3)$$

$$\frac{\eta_2}{E_{22}} = \frac{V_{CNT}}{E_{22}^{CNT}} + \frac{V_m}{E^m}, \quad (4)$$

$$\frac{\eta_3}{G_{12}} = \frac{V_{CNT}}{G_{12}^{CNT}} + \frac{V_m}{G^m}, \quad (5)$$

where  $E_{11}^{CNT}$  and  $E_{22}^{CNT}$  are the Young's moduli of CNT in longitudinal and transverse directions, respectively.  $G_{12}^{CNT}$  is the shear modulus of CNT.  $E^m$  and  $G^m$  are the corresponding properties of the isotropic matrix. As the load transfer between the nanotube and matrix is less than perfect, Shen [23] introduced  $\eta_j$  ( $j = 1, 2, 3$ ), called CNT efficiency parameters, into Eqs. (3)–(5) to account load transfer between the nanotubes and polymeric phases (e.g. the surface effect, strain gradient effect, and intermolecular coupled effect) and other effects on the effective material properties of CNTRCs.  $V_{CNT}$  and  $V_m$  are the CNT and matrix volume fractions. Since Poisson's ratio depends weakly on the position, we assume  $\nu_{12}$  to be

$$\nu_{12} = V_{CNT}^* \nu_{12}^{CNT} + V_m \nu^m, \quad (6)$$

where  $\nu_{12}^{CNT}$  and  $\nu^m$  are Poisson's ratios of CNTs and the matrix, respectively. Similarly, thermal expansion coefficients are also assumed to be graded in the thickness direction and are expressed as

$$\alpha_{11} = V_{CNT} \alpha_{11}^{CNT} + V_m \alpha^m, \quad (7)$$

$$\alpha_{22} = (1 + \nu_{12}^{CNT}) V_{CNT} \alpha_{22}^{CNT} + (1 + \nu^m) V_m \alpha^m - \nu_{12} \alpha_{11}, \quad (8)$$

where  $\alpha_{11}^{CNT}$  and  $\alpha_{22}^{CNT}$  are thermal expansion coefficients of the CNTs in the longitudinal and transverse directions, respectively.  $\alpha^m$  is the expansion coefficient of the matrix.

### 2.2. Eshelby–Mori–Tanaka approach

The Eshelby–Mori–Tanaka approach, known as the equivalent inclusion-average stress method, is based on the equivalent elastic inclusion idea of Eshelby [51,52] and the concept of average stress in the matrix due to Mori–Tanaka [53]. According to Benveniste's revision [54], the tensor of effective elastic moduli  $\mathbf{C}$  of CNTRCs is given by

$$\mathbf{C} = \mathbf{C}_m + V_{CNT} (\mathbf{C}_{CNT} - \mathbf{C}_m) \cdot \mathbf{A} \cdot [V_m \mathbf{I} + V_{CNT} \langle \mathbf{A} \rangle]^{-1}, \quad (9)$$

where  $\mathbf{I}$  is the fourth-order unit tensor.  $\mathbf{C}_m$  and  $\mathbf{C}_{CNT}$  are the stiffness tensors of the matrix and CNT, respectively. It should be note that the brackets represent an average overall possible orientation of the inclusions.  $\mathbf{A}$  is the dilute mechanical strain concentration tensor and is given by

$$\mathbf{A} = [\mathbf{I} + \mathbf{S} \cdot \mathbf{C}_m^{-1} \cdot (\mathbf{C}_{CNT} - \mathbf{C}_m)]^{-1}, \quad (10)$$

where  $\mathbf{S}$  is the fourth-order Eshelby tensor [52] which is specialized to the case of cylindrical inclusions representative of the CNTs and depends on their orientation by Mura [55].

## 3. Theoretical formulations

### 3.1. Energy functional

According to the first-order shear deformation theory [56], the displacement field can be expressed as

$$u(x, y, z) = u_0(x, y) + z\phi_x(x, y), \quad (11)$$

$$v(x, y, z) = v_0(x, y) + z\phi_y(x, y), \quad (12)$$

$$w(x, y, z) = w_0(x, y), \quad (13)$$

where  $u_0$ ,  $v_0$  and  $w_0$  represent the respective translation displacements of a point at the mid-plane of the plate in  $x$ ,  $y$  and  $z$

directions;  $\phi_x$  and  $\phi_y$  denote rotations of a transverse normal about positive  $y$  and negative  $x$  axes, respectively. The linear strain–displacement relationships are given by

$$\begin{Bmatrix} \varepsilon_{xx} \\ \varepsilon_{yy} \\ \gamma_{xy} \end{Bmatrix} = \boldsymbol{\varepsilon}_0 + \mathbf{Z}\boldsymbol{\kappa}, \quad \begin{Bmatrix} \gamma_{yz} \\ \gamma_{xz} \end{Bmatrix} = \boldsymbol{\gamma}_0, \quad (14)$$

where

$$\boldsymbol{\varepsilon}_0 = \begin{Bmatrix} \frac{\partial u_0}{\partial x} \\ \frac{\partial v_0}{\partial y} \\ \frac{\partial u_0}{\partial y} + \frac{\partial v_0}{\partial x} \end{Bmatrix}, \quad \boldsymbol{\kappa} = \begin{Bmatrix} \frac{\partial \phi_x}{\partial x} \\ \frac{\partial \phi_y}{\partial y} \\ \frac{\partial \phi_x}{\partial y} + \frac{\partial \phi_y}{\partial x} \end{Bmatrix}, \quad \boldsymbol{\gamma}_0 = \begin{Bmatrix} \phi_y + \frac{\partial w_0}{\partial y} \\ \phi_x + \frac{\partial w_0}{\partial x} \end{Bmatrix}. \quad (15)$$

Then, the linear constitutive relations are expressed as

$$\begin{Bmatrix} \sigma_{xx} \\ \sigma_{yy} \\ \sigma_{xy} \\ \sigma_{yz} \\ \sigma_{xz} \end{Bmatrix} = \begin{bmatrix} Q_{11} & Q_{12} & 0 & 0 & 0 \\ Q_{12} & Q_{22} & 0 & 0 & 0 \\ 0 & 0 & Q_{66} & 0 & 0 \\ 0 & 0 & 0 & Q_{44} & 0 \\ 0 & 0 & 0 & 0 & Q_{55} \end{bmatrix} \begin{Bmatrix} \varepsilon_{xx} \\ \varepsilon_{yy} \\ \gamma_{xy} \\ \gamma_{yz} \\ \gamma_{xz} \end{Bmatrix} - \begin{Bmatrix} \alpha_{11} \\ \alpha_{22} \\ 0 \\ 0 \\ 0 \end{Bmatrix} \Delta T, \quad (16)$$

where

$$Q_{11} = \frac{E_{11}}{1 - \nu_{12}\nu_{21}}, \quad Q_{22} = \frac{E_{22}}{1 - \nu_{12}\nu_{21}}, \quad Q_{12} = \frac{\nu_{21}E_{11}}{1 - \nu_{12}\nu_{21}}, \quad (17)$$

$$Q_{66} = G_{12}, \quad Q_{44} = G_{23}, \quad Q_{55} = G_{13}, \quad (18)$$

and  $\Delta T$  is the temperature change with respect to a reference state.  $E_{11}$  and  $E_{22}$  are effective Young's moduli of CNTRC plates in the principal material coordinate;  $G_{12}$ ,  $G_{13}$  and  $G_{23}$  are the shear moduli; and  $\nu_{12}$  and  $\nu_{21}$  are Poisson's ratios.

The strain energy of the plate is expressed by

$$U_\varepsilon = \frac{1}{2} \int_\Omega \boldsymbol{\varepsilon}^T \mathbf{S} \boldsymbol{\varepsilon} d\Omega, \quad (19)$$

where

$$\boldsymbol{\varepsilon} = \begin{Bmatrix} \boldsymbol{\varepsilon}_0 \\ \boldsymbol{\kappa} \\ \boldsymbol{\gamma}_0 \end{Bmatrix}, \quad (20)$$

$$\mathbf{S} = \begin{bmatrix} A_{11} & A_{12} & A_{16} & B_{11} & B_{12} & B_{16} & 0 & 0 \\ A_{12} & A_{22} & A_{26} & B_{12} & B_{22} & B_{26} & 0 & 0 \\ A_{16} & A_{26} & A_{66} & B_{16} & B_{26} & B_{66} & 0 & 0 \\ B_{11} & B_{12} & B_{16} & D_{11} & D_{12} & D_{16} & 0 & 0 \\ B_{12} & B_{22} & B_{26} & D_{12} & D_{22} & D_{26} & 0 & 0 \\ B_{16} & B_{26} & B_{66} & D_{16} & D_{26} & D_{66} & 0 & 0 \\ 0 & 0 & 0 & 0 & 0 & 0 & A_{44}^s & A_{45}^s \\ 0 & 0 & 0 & 0 & 0 & 0 & A_{45}^s & A_{55}^s \end{bmatrix} = \begin{bmatrix} \mathbf{A} & \mathbf{B} & \mathbf{0} \\ \mathbf{B} & \mathbf{D} & \mathbf{0} \\ \mathbf{0} & \mathbf{0} & \mathbf{A}_s \end{bmatrix}, \quad (21)$$

in which the extensional  $A_{ij}$ , coupling  $B_{ij}$ , bending  $D_{ij}$ , and transverse shear  $A_{ij}^s$  stiffness are given by

$$(A_{ij}, B_{ij}, D_{ij}) = \int_{-h/2}^{h/2} Q_{ij}(1, z, z^2) dz, \quad A_{ij}^s = K \int_{-h/2}^{h/2} Q_{ij} dz, \quad (22)$$

where  $i, j = 1, 2, 6$  in  $A_{ij}$ ,  $B_{ij}$  and  $D_{ij}$  and  $i, j = 4, 5$  in  $A_{ij}^s$ .  $K$  denotes the transverse shear correction coefficient, which is taken to be  $K = 5/6$  for isotropic materials. For FGMs, the shear correction coefficient is suggested as  $K = 5/(6 - (\nu_1 V_1 + \nu_2 V_2))$ , by Efraim and Eisenberger [57].

Kinetic energy of the plates for free vibration analysis is given by

$$\Theta = \frac{1}{2} \int_\Omega \int_{-h/2}^{h/2} \rho(z) (\dot{u}^2 + \dot{v}^2 + \dot{w}^2) dz d\Omega. \quad (23)$$

Therefore, the total energy function for the plate can be expressed as

$$\Pi_s = U_\varepsilon - \Theta. \quad (24)$$

### 3.2. Two-dimensional kernel particle shape functions

Theoretical formulation of the reproducing kernel particle method (RKPM) has been given in detail by Liu et al. [58] and Chen et al. [43]. Construction of the shape function in RKPM is briefly reviewed here. For a domain discretized by a set of nodes  $\mathbf{x}_I$ ,  $I = 1, \dots, NP$ , displacement approximations are expressed in the discrete form

$$u^h = \sum_{I=1}^{NP} \psi_I(\mathbf{x}) \mathbf{u}_I, \quad (25)$$

where  $\psi_I(\mathbf{x})$  and  $\mathbf{u}_I$  are the shape function and nodal parameter associated with node  $I$ , respectively.

The two-dimensional shape function is expressed as

$$\psi_I(\mathbf{x}) = C(\mathbf{x}; \mathbf{x} - \mathbf{x}_I) \Phi_a(\mathbf{x} - \mathbf{x}_I), \quad (26)$$

where  $\Phi_a(\mathbf{x} - \mathbf{x}_I)$  is the kernel function, and  $C(\mathbf{x}; \mathbf{x} - \mathbf{x}_I)$  is the correction function, which is used to satisfy the reproduction conditions

$$\sum_{I=1}^{NP} \psi_I(\mathbf{x}) x_I^p y_I^q = x^p y^q \quad \text{for } p + q = 0, 1, 2. \quad (27)$$

The correction function is expressed by a linear combination of polynomial basis functions

$$C(\mathbf{x}; \mathbf{x} - \mathbf{x}_I) = \mathbf{H}^T(\mathbf{x} - \mathbf{x}_I) \mathbf{b}(\mathbf{x}), \quad (28)$$

$$\mathbf{b}(\mathbf{x}) = [b_0(x, y), b_1(x, y), b_2(x, y), b_3(x, y), b_4(x, y), b_5(x, y)]^T, \quad (29)$$

$$\mathbf{H}^T(\mathbf{x} - \mathbf{x}_I) = [1, x - x_I, y - y_I, (x - x_I)(y - y_I), (x - x_I)^2, (y - y_I)^2], \quad (30)$$

where  $\mathbf{H}$  is a vector of the quadratic basis and  $\mathbf{b}(\mathbf{x})$  is a coefficient function of  $x$  and  $y$  are to be determined. Then, the shape function can be written as

$$\psi_I(\mathbf{x}) = \mathbf{b}^T(\mathbf{x}) \mathbf{H}(\mathbf{x} - \mathbf{x}_I) \Phi_a(\mathbf{x} - \mathbf{x}_I). \quad (31)$$

By substituting Eq. (31) into Eq. (27), we can obtain coefficient  $\mathbf{b}(\mathbf{x})$  as

$$\mathbf{b}(\mathbf{x}) = \mathbf{M}^{-1}(\mathbf{x}) \mathbf{H}(\mathbf{0}), \quad (32)$$

where

$$\mathbf{M}(\mathbf{x}) = \sum_{I=1}^{NP} \mathbf{H}(\mathbf{x} - \mathbf{x}_I) \mathbf{H}^T(\mathbf{x} - \mathbf{x}_I) \Phi_a(\mathbf{x} - \mathbf{x}_I), \quad (33)$$

$$\mathbf{H}(\mathbf{0}) = [1, 0, 0, 0, 0, 0]^T. \quad (34)$$

For this 2-D plate problem, kernel function  $\Phi_a(\mathbf{x} - \mathbf{x}_I)$  is defined as

$$\Phi_a(\mathbf{x} - \mathbf{x}_I) = \Phi_a(x) \cdot \Phi_a(y), \quad (35)$$

in which

$$\Phi_a(x) = \varphi\left(\frac{x - x_I}{a}\right), \quad (36)$$

where  $\varphi(x)$  is the weight function. The cubic spline function is chosen as the weight function, and is given by

$$\varphi_z(z_I) = \begin{cases} \frac{2}{3} - 4z_I^2 + 4z_I^3 & \text{for } 0 \leq |z_I| \leq \frac{1}{2} \\ \frac{4}{3} - 4z_I + 4z_I^2 - \frac{4}{3}z_I^3 & \text{for } \frac{1}{2} < |z_I| \leq 1 \\ 0 & \text{otherwise} \end{cases}, \quad (37)$$

where  $z_I = \frac{x - x_I}{d_I}$ ,  $d_I$  is the size of the support of node  $I$ , calculated by  $d_I = d_{\max} c_I$ ,  $(38)$

**Table 1**Material properties of (10, 10) SWCNT ( $L = 9.26$  nm,  $R = 0.68$  nm,  $h = 0.067$  nm,  $\nu_1^{CNT} = 0.175$ ).

Temperature (K)	$E_{11}^{CNT}$ (TPa)	$E_{22}^{CNT}$ (TPa)	$G_{12}^{CNT}$ (TPa)	$\alpha_{11}^{CNT}$ ( $10^{-6}/K$ )	$\alpha_{22}^{CNT}$ ( $10^{-6}/K$ )
300	5.6466	7.0800	1.9445	3.4584	5.1682
500	5.5308	6.9348	1.9643	4.5361	5.0189
700	5.4744	6.8641	1.9644	4.6677	4.8943

where  $d_{max}$  is a scaling factor ranging from 2.0 to 4.0. Distance  $c_i$  is chosen by searching for enough nodes to avoid the singularity of matrix  $\mathbf{M}$ .

Eventually, the shape function is expressed as

$$\psi_I(\mathbf{x}) = \mathbf{H}^T(\mathbf{0})\mathbf{M}^{-1}(\mathbf{x})\mathbf{H}(\mathbf{x} - \mathbf{x}_I)\Phi_a(\mathbf{x} - \mathbf{x}_I). \quad (39)$$

The boundary conditions cannot be directly imposed because the shape function does not have Kronecker delta property. Several methods, such as the transformation method [43], Lagrange multipliers [34] and the penalty method, are useful for enforcing the essential boundary conditions.

### 3.3. Discrete system equations

For a plate discretized by a set of nodes  $\mathbf{x}_I$ ,  $I = 1, \dots, NP$ , approximations of displacements are expressed as

$$\mathbf{u}_0^h = \begin{pmatrix} u_0^h \\ v_0^h \\ w_0^h \\ \phi_x^h \\ \phi_y^h \end{pmatrix} = \sum_{I=1}^{NP} \psi_I \begin{pmatrix} u_I \\ v_I \\ w_I \\ \phi_{xI} \\ \phi_{yI} \end{pmatrix} \mathbf{e}^{i\omega t} = \sum_{I=1}^{NP} \psi_I(\mathbf{x}) \mathbf{u}_I \mathbf{e}^{i\omega t}. \quad (40)$$

The transformation method is employed to enforce the essential boundary conditions in this paper. By substituting Eq. (40) into Eq. (24) and taking the variation in the energy function yields the free vibration eigen-equation

$$(\tilde{\mathbf{K}} - \omega^2 \tilde{\mathbf{M}}) \tilde{\mathbf{u}} = 0, \quad (41)$$

where

$$\tilde{\mathbf{K}} = \Lambda^{-1} \mathbf{K} \Lambda^{-T}, \quad \tilde{\mathbf{M}} = \Lambda^{-1} \bar{\mathbf{M}} \Lambda^{-T}, \quad \tilde{\mathbf{u}} = \Lambda^T \mathbf{u}, \quad (42)$$

$$\mathbf{K} = \mathbf{K}^b + \mathbf{K}^m + \mathbf{K}^s, \quad (43)$$

in which  $\mathbf{K}$  denotes the linear stiffness matrix and  $\Lambda$  is the transformation matrix.

Matrices  $\Lambda$ ,  $\mathbf{K}^b$ ,  $\mathbf{K}^m$ ,  $\mathbf{K}^s$ ,  $\mathbf{u}$ , and  $\bar{\mathbf{M}}$  are given as follows:

$$\Lambda_{ij} = \psi_I(\mathbf{x}_j) \mathbf{I}, \quad \mathbf{I} \text{ is the identity matrix} \quad (44)$$

$$\mathbf{u} = [u_1 \ u_2 \ \dots \ u_n]^T, \quad (45)$$

$$\mathbf{K}_{ij}^b = \int_{\Omega} (\mathbf{B}_i^b)^T \mathbf{D} \mathbf{B}_j^b d\Omega, \quad (46)$$

$$\mathbf{K}_{ij}^m = \int_{\Omega} (\mathbf{B}_i^m)^T \mathbf{A} \mathbf{B}_j^m d\Omega + \int_{\Omega} (\mathbf{B}_i^m)^T \bar{\mathbf{B}} \mathbf{B}_j^b d\Omega + \int_{\Omega} (\mathbf{B}_i^b)^T \bar{\mathbf{B}} \mathbf{B}_j^m d\Omega, \quad (47)$$

$$\mathbf{K}_{ij}^s = \int_{\Omega} (\mathbf{B}_i^s)^T \mathbf{A}^s \mathbf{B}_j^s d\Omega, \quad (48)$$

$$\bar{\mathbf{M}} = \int_{\Omega} \mathbf{G}_i^T \bar{\mathbf{m}} \mathbf{G}_j d\Omega, \quad (49)$$

where

$$\mathbf{B}_i^b = \begin{bmatrix} 0 & 0 & 0 & \frac{\partial \psi_I}{\partial x} & 0 \\ 0 & 0 & 0 & 0 & \frac{\partial \psi_I}{\partial y} \\ 0 & 0 & 0 & \frac{\partial \psi_I}{\partial y} & \frac{\partial \psi_I}{\partial x} \end{bmatrix}, \quad \mathbf{B}_i^m = \begin{bmatrix} \frac{\partial \psi_I}{\partial x} & 0 & 0 & 0 & 0 \\ 0 & \frac{\partial \psi_I}{\partial y} & 0 & 0 & 0 \\ \frac{\partial \psi_I}{\partial y} & \frac{\partial \psi_I}{\partial x} & 0 & 0 & 0 \end{bmatrix}, \quad (50)$$

$$\mathbf{B}_i^s = \begin{bmatrix} 0 & 0 & \frac{\partial \psi_I}{\partial x} & \psi_I & 0 \\ 0 & 0 & \frac{\partial \psi_I}{\partial y} & 0 & \psi_I \end{bmatrix},$$

$$\mathbf{G}_I = \begin{bmatrix} \psi_I & 0 & 0 & 0 & 0 \\ 0 & \psi_I & 0 & 0 & 0 \\ 0 & 0 & \psi_I & 0 & 0 \\ 0 & 0 & 0 & \psi_I & 0 \\ 0 & 0 & 0 & 0 & \psi_I \end{bmatrix}, \quad \bar{\mathbf{m}} = \begin{bmatrix} I_0 & 0 & 0 & I_1 & 0 \\ 0 & I_0 & 0 & 0 & I_1 \\ 0 & 0 & I_0 & 0 & 0 \\ I_1 & 0 & 0 & I_2 & 0 \\ 0 & I_1 & 0 & 0 & I_2 \end{bmatrix}, \quad (51)$$

Matrices  $\mathbf{A}$ ,  $\bar{\mathbf{B}}$ ,  $\mathbf{D}$  and  $\mathbf{A}^s$  can be calculated using either an analytical or a numerical method. Matrices  $\mathbf{K}^b$  and  $\mathbf{K}^m$  are evaluated with a  $4 \times 4$  Gauss integration and shear stiffness  $\mathbf{K}^s$  is obtained by a one-point Gauss integration.  $I_0$ ,  $I_1$  and  $I_2$  are normal, coupled normal-rotary and rotary inertial coefficients, which are defined by

$$(I_0, I_1, I_2) = \int_{-2/h}^{h/2} \rho(z) (1, z, z^2) dz. \quad (52)$$

## 4. Numerical results

In this section, several numerical examples are presented to explicate free vibration frequency characteristics of FG-CNTRC plates. Poly{(m-phenylenevinylene)-co-[(2,5-dioctoxy-p-phenylene) vinylene]} referred as PmPV [59] is selected for the matrix. Material properties of PmPV are assumed to be  $\nu^m = 0.34$  and  $E^m = (3.51 - 0.0047T)$  GPa, where  $T = T_0 + \Delta T$  and  $T_0 = 300$  K (room temperature). When  $T = 300$  K,  $E^m = 2.1$  GPa. The (10, 10) SWCNTs are selected as reinforcement for the present study. As reported in the literature, chirality, size and temperature of SWCNT can significantly affect material properties of SWCNTs [60–63]. Also the effective thickness of CNT plays an important role in estimating the effective material properties of CNTs. With the effective thickness of CNTs is assumed to be 0.34 nm, Han and Elliott [49] obtained a low value of modulus for (10, 10) SWCNTs ( $E_{11}^{CNT} = 600$  GPa,  $E_{22}^{CNT} = 10$  GPa,  $G_{12}^{CNT} = 17.2$  GPa). However, Wang and Zhang [64] reported recently that the effective thickness of SWCNTs should be smaller than 0.142 nm. Thus, all material properties of SWCNTs used for present analysis of FG-CNTRC plates are selected from MD simulation results reported by Zhang and Shen [18] where the effective wall thickness obtained for (10, 10) SWCNTs is 0.067 nm, which satisfies the Vodenitcharova–Zhang criterion.[64]. Typical values of effective material properties of (10, 10) SWCNTs are listed in Table 1. The effective material properties of CNTRCs can be estimated by either the Eshelby–Mori–Tanaka approach or the extended rule of mixture. In this paper, the extended rule of mixture is applied to predict the effective material properties of CNTRCs for the convergence and comparison studies and the Eshelby–Mori–Tanaka approach is used for detailed parametric study. The shape function of 2-D displacement approximations is constructed with the kernel particle function. Each of the edges of the plates may be simply supported (S), fully clamped (S) or free (F). A sequence of letters containing “S”, “C” or “F” is used to denote the essential boundary conditions of four edges. The non-dimensional frequency parameter is defined as

$$\bar{\omega}_{mn} = \omega_{mn} \frac{b^2}{h} \sqrt{\frac{\rho^m}{E^m}}, \quad (53)$$

where  $\omega_{mn}$  is the natural frequency of the CNTRC plates. Subscripts  $m$  and  $n$  are the number of half-waves of mode shapes in  $x$  and  $y$  directions, respectively.

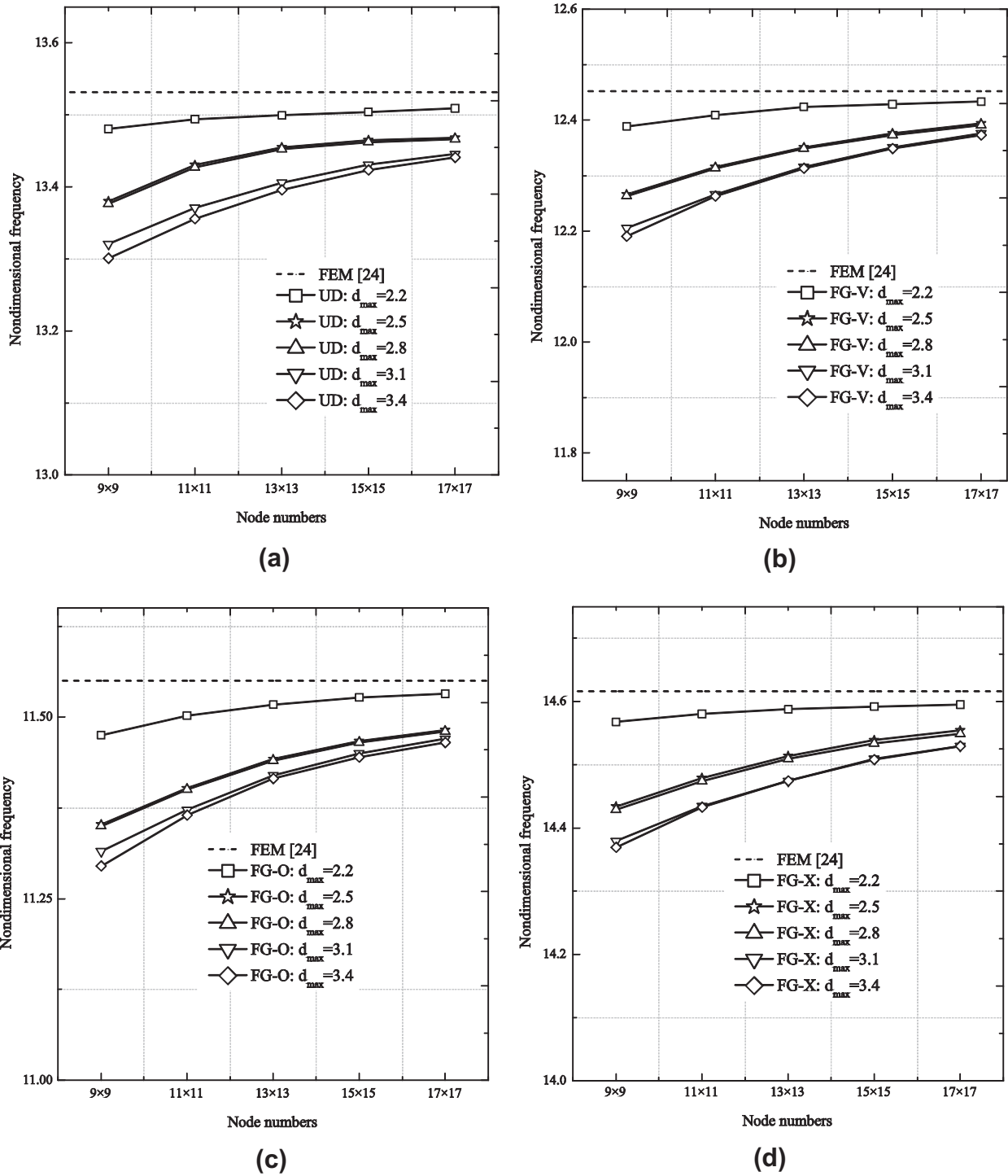


Fig. 2. Convergence properties of various types of CNTRC plates in terms of the number of nodes with different support sizes. (a) UD; (b) FG-V; (c) FG-O; and (d) FG-X.

4.1. Convergence and comparison studies

Convergence properties for free vibration analysis of CNTRC plates are studied in terms of the number of nodes with different support sizes to verify the accuracy and efficiency of the proposed method. The extended rule of mixture is applied to predict effective material properties of CNTRCs. Determining the CNT efficiency parameter is very important to apply the rule of mixture to estimate effective material properties of CNTRCs. Shen

[23] determined the CNT efficiency parameter by matching Young's moduli  $E_{11}$  and  $E_{22}$  of CNTRCs obtained by the extended rule of mixture to MD results of Han and Elliott [59]. The boundary condition of CNTRC plates is four edges simply supported (SSSS). As shown in Fig. 2, it can be seen that the present non-dimensional fundamental frequency ( $m = n = 1$ ) matches very well with ANSYS results (SHELL181 element for UD-CNTRC plates and SHELL99 element for FG-CNTRC plates) [24]. When plates are represented by  $17 \times 17$  nodes and a scaling factor

**Table 2**  
Non-dimensional natural frequency for simply supported and four edges fully clamped various types of CNTRC plates.

Boundary condition	Mode	UD		FG-V		FG-O		FG-X	
		Present	FEM [24]						
SSSS	1	13.495	13.532	12.416	12.452	11.514	11.550	14.578	14.616
	2	17.629	17.700	16.984	17.060	16.187	16.265	18.579	18.646
	3	19.399	19.449	19.448	19.499	19.449	19.499	19.449	19.499
	4	19.404	19.449	19.452	19.499	19.454	19.499	19.454	19.499
	5	27.307	27.569	27.069	27.340	26.240	26.513	28.261	28.519
	6	32.466	32.563	31.309	31.417	30.163	30.280	33.510	33.598
CCCC	1	17.587	17.625	17.171	17.211	16.667	16.707	18.045	18.083
	2	22.933	23.041	22.704	22.818	22.138	22.253	23.498	23.606
	3	33.170	33.592	32.939	33.070	32.237	32.378	33.915	34.338
	4	33.612	33.729	33.121	33.552	32.424	32.857	34.361	34.467
	5	36.905	37.011	36.405	36.528	35.674	35.809	37.367	37.447
	6	37.238	37.317	37.357	37.437	37.367	37.447	37.693	37.786

**Table 3**  
Non-dimensional natural frequency for simply supported various types of CNTRC plates in different temperature environments.

Temperature	Mode	UD		FG-V		FG-O		FG-X	
		Present	Wang [66]	Present	Wang [66]	Present	–	Present	–
300 K	1	12.1261	12.2696	11.3095	11.3074	10.4535	–	13.1289	–
	2	16.5545	16.8071	16.2611	16.1790	15.3530	–	17.1045	–
	3	16.9835	–	17.0406	–	17.0365	–	17.3901	–
	4	26.0723	–	25.9239	–	17.0417	–	26.9635	–
	5	28.3715	29.4399	27.8895	28.3821	26.5257	–	29.6804	–
	6	30.6458	–	29.9585	–	29.0558	–	31.5033	–
500 K	1	10.9644	11.0402	10.2442	10.2068	9.5378	–	11.6675	–
	2	14.4941	14.7052	14.2264	14.1873	13.4627	–	14.5948	–
	3	14.5494	–	14.5404	–	14.5394	–	15.1371	–
	4	22.4220	–	22.2866	–	21.6279	–	23.1611	–
	5	25.0803	25.8619	24.4494	25.1033	23.4080	–	25.6915	–
	6	26.5461	–	26.0737	–	25.4096	–	27.1711	–
700 K	1	9.2518	9.3611	8.7751	8.8190	8.2728	–	9.6982	–
	2	11.5159	12.0533	11.5436	11.6928	11.1033	–	11.5519	–
	3	11.8279	–	11.5514	–	11.5090	–	12.2867	–
	4	17.9433	–	17.8435	–	17.3375	–	18.4932	–
	5	20.3060	21.3606	19.9708	20.9137	19.2831	–	20.6604	–
	6	21.3761	–	21.1273	–	20.7209	–	21.7653	–

**Table 4**  
Non-dimensional natural frequency of various types of simply supported CNTRC plates with different estimations of effective material properties.

Types	Mode	Mode					
		1	2	3	4	5	6
UD	Extended rule of mixture	13.1507	17.9875	19.8236	19.9500	28.9201	32.7653
	Eshelby–Mori–Tanaka	12.7824	17.5016	19.0806	19.1034	27.9322	31.3902
FG-V	Extended rule of mixture	12.0357	17.4121	19.7355	19.9088	28.9056	31.0341
	Eshelby–Mori–Tanaka	11.6600	16.8445	19.0811	19.1044	27.6270	29.9925
FG-O	Extended rule of mixture	11.2171	16.8332	19.7047	19.7846	28.1450	29.7256
	Eshelby–Mori–Tanaka	10.8016	16.1833	18.9034	18.9061	27.0305	28.7640
FG-X	Extended rule of mixture	14.2839	19.0014	19.9876	20.0054	30.9261	33.8798
	Eshelby–Mori–Tanaka	13.8742	18.3303	19.0834	19.1061	29.6183	32.4900

$d_{\max} = 2.2$  is used, the maximum difference is only 0.55%. According to its effectiveness and efficiency, discretization with  $17 \times 17$  nodes and a scaling factor  $d_{\max} = 2.2$  have been used for all further analyses. The first comparison study is carried out for simply supported and four edges fully clamped various types of CNTRC plates, and typical results are shown in Table 2. It can be seen that the present results agree well with FEM results reported by Zhu et al. [24]. Table 3 shows a further comparison for simply supported various types of CNTRC plates in

different temperature environments. A good agreement is also obtained between the present results and the solutions given by Wang and Shen [65].

#### 4.2. Parameter studies

Several numerical examples showing the applicability of the element-free  $kp$ -Ritz method on free vibration analysis of CNTRC plates are presented in this section. The effective material

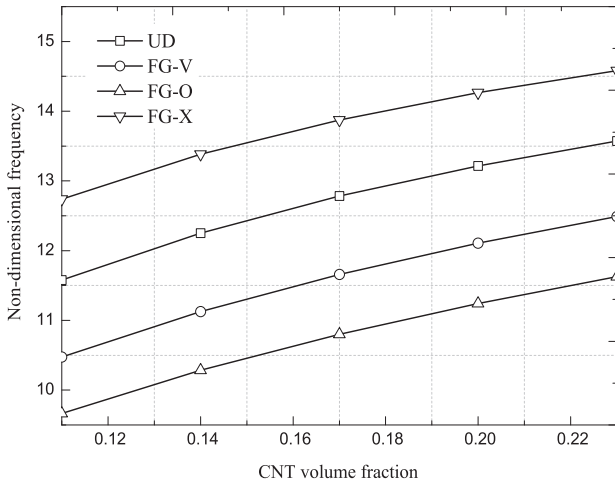


**Fig. 3.** Variation of non-dimensional fundamental frequency  $\bar{\omega} = \omega \frac{b^2}{h} \sqrt{\frac{\rho^m}{E^m}}$  of simply supported various types of CNTRC plates versus the CNT volume fraction.

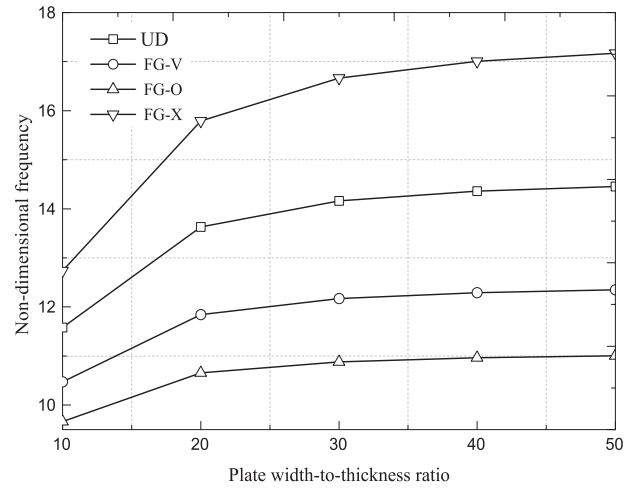


**Fig. 5.** Variation of non-dimensional fundamental frequency  $\bar{\omega} = \omega \frac{b^2}{h} \sqrt{\frac{\rho^m}{E^m}}$  of simply supported various types of CNTRC plates versus the plate width-to-thickness ratio.

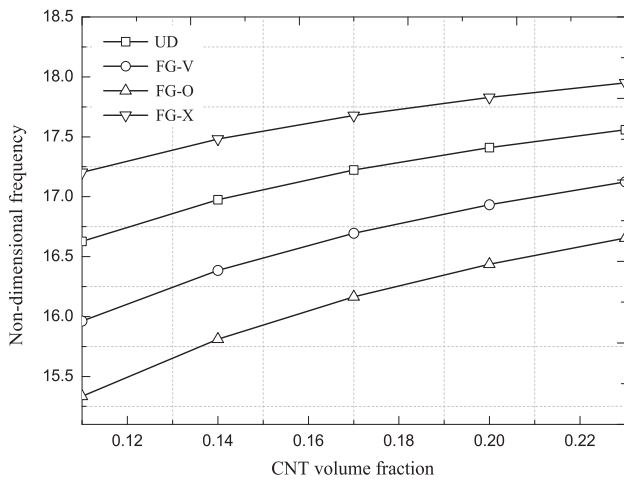


**Fig. 4.** Variation of non-dimensional fundamental frequency  $\bar{\omega} = \omega \frac{b^2}{h} \sqrt{\frac{\rho^m}{E^m}}$  of four edges fully clamped various types of CNTRC plates versus the CNT volume fraction.

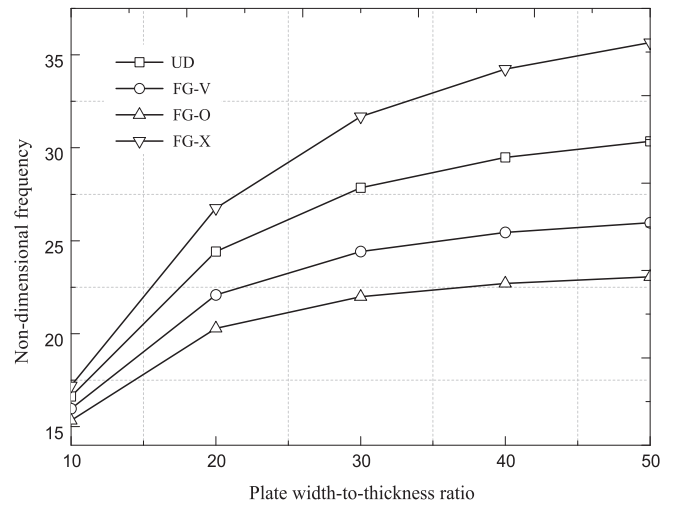


**Fig. 6.** Variation of non-dimensional fundamental frequency  $\bar{\omega} = \omega \frac{b^2}{h} \sqrt{\frac{\rho^m}{E^m}}$  of four edges fully clamped various types of CNTRC plates versus the plate width-to-thickness ratio.

properties of CNTRCs are estimated by the Eshelby–Mori–Tanaka approach. Here detailed parametric studies are carried out to investigate the effects of CNT volume fraction, plate width-to-thickness ratio, plate aspect ratio, and boundary condition on frequency characteristics of various types of CNTRC plates.

Table 4 shows the non-dimensional fundamental frequency of various types of simply supported CNTRC plates with the effective material properties of CNTRCs plates estimated by both the extended rule of mixture and Eshelby–Mori–Tanaka approach. The plate width-to-thickness ratio  $b/h$  is assumed to be 10. The CNT volume fraction  $V_{CNT}^*$  is selected as 0.17. It can be seen that the non-dimensional fundamental frequency obtained by the extended rule of mixture agrees well with solution of Eshelby–Mori–Tanaka approach. Compared with the results, we also found that results obtained by the extended rule of mixture are a little higher than those of Eshelby–Mori–Tanaka approach.

Figs. 3 and 4 show the effect of CNT volume fraction on non-dimensional fundamental frequency of various types of CNTRC plates with simply supported and four edges fully clamped boundary conditions. It is found that the non-dimensional fundamental frequency of the plates has a higher value with a larger volume

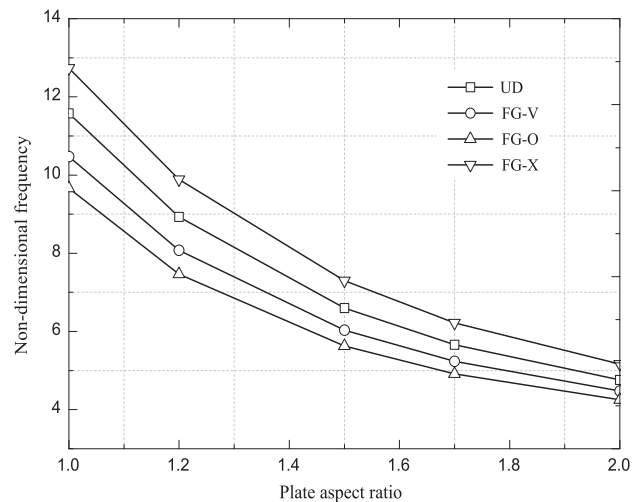


**Fig. 7.** Variation of non-dimensional fundamental frequency  $\bar{\omega} = \omega \frac{b^2}{h} \sqrt{\frac{\rho^m}{E^m}}$  of simply supported various types of CNTRC plates versus the plate aspect ratio.

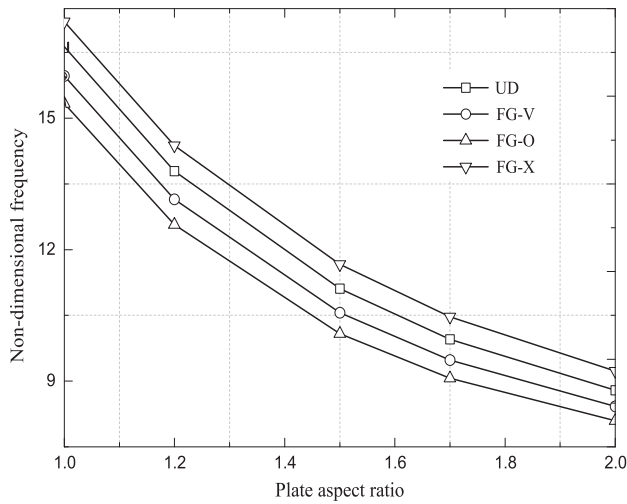


Fig. 8. Variation of non-dimensional fundamental frequency  $\bar{\omega} = \omega \frac{b^2}{h} \sqrt{\frac{\rho}{E_m}}$  of four edges fully clamped various types of CNTRC plates versus the plate aspect ratio.

fraction of CNT since the stiffness of CNTRC plates is larger when the value of CNT volume fraction is higher. It is worth to note that FG-X plates have the highest value of frequency and FG-O plates have the lowest value of frequency among the plates due to reinforcements distributed close to top and bottom are more efficient than those distributed near the mid-plane for increasing the stiffness of CNTRC plates [24]. Some similar observations can also be discerned from Figs. 5 and 6, which depict the variation of non-dimensional fundamental frequency of simply supported and four edges fully clamped various types of CNTRC plates with plate width-to-thickness ratio. It can be found that as the plate width-to-thickness ratio increases, the non-dimensional fundamental natural frequency becomes less sensitive to the change of plate

width-to-thickness ratio for UN-CNTRC plates and the other three types of FG-CNTRC plates.

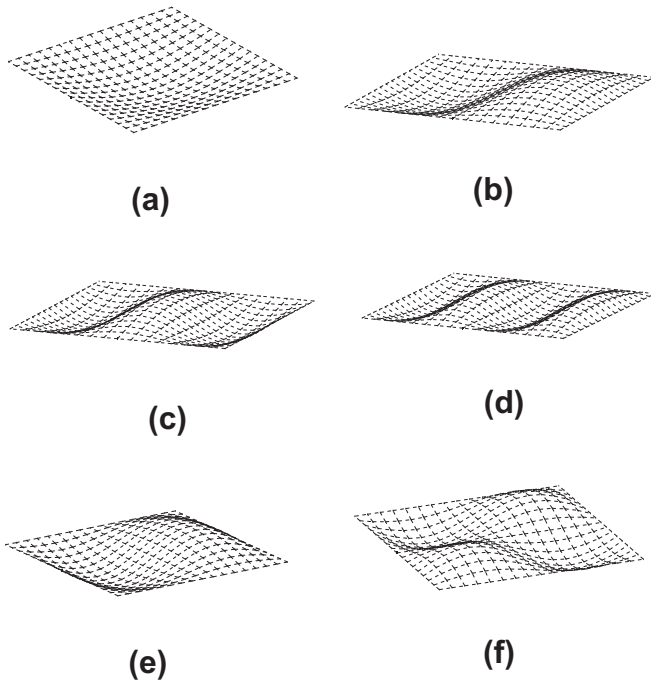
Figs. 7 and 8 show the variation of non-dimensional fundamental natural frequency of simply supported and four edges fully clamped various types of CNTRC plates with the plate aspect ratio ( $\beta = a/b$ ) changing from 1.0 to 2.0. The plate width-to-thickness ratio is set to be  $b/h = 10$  and CNT volume fraction  $V_{CNT}^* = 0.11$  is considered. It can be seen that the non-dimensional fundamental frequency decreases as  $\beta$  increases for UN-CNTRC plates and the other three types of FG-CNTRC plates. A similar effect of the distribution types of CNTs in the plate can also be obtained when we change the plate aspect ratio.

Table 5 lists results of various types of CNTRC plates with different boundary conditions. It can be seen that the value of non-dimensional fundamental natural frequency of CNTRC plates with CCCC boundary condition is the highest and the minimum non-dimensional fundamental natural frequency is occurred for CNTRC plates with SFSF boundary condition. That is to be expected, because the constraint of boundary condition clamped (C) is stronger than boundary condition supported (S) and boundary condition free (F) has no constraint of the edges.

Fig. 9 shows the first six mode shapes of four edges fully clamped FG-V CNTRC plate ( $V_{CNT}^* = 0.11, b/h = 50$ ). Mechanical properties of CNTRC plates are much higher in the longitudinal direction (in x axis) than in the transverse direction (in y axis) since CNTs only align in x direction. Then the mode sequence of this CNTRC plate is dissimilar to that of an isotropic plate, compared with mode shapes of isotropic Mindlin/Reissner plate given in [41]. For isotropic Mindlin/Reissner plate mode ( $m = 2, n = 1$ ) and mode ( $m = 2, n = 2$ ) are in the lower order than mode ( $m = 1, n = 3$ ) and mode ( $m = 1, n = 4$ ). For present CNTRC plates, we can discovered that mode ( $m = 2, n = 1$ ) and mode ( $m = 2, n = 2$ ) become of higher order over mode ( $m = 1, n = 3$ ) and mode ( $m = 1, n = 4$ ) due to the much higher mechanical properties of CNTRC plates in the longitudinal direction.

Table 5 Effect of boundary conditions on non-dimensional natural frequency for various types of CNTRC plates.

Mode	Boundary conditions						
	SSSS	CCCC	SCSC	SFSF	CCCF	SSSF	
UD	1	11.580	16.627	12.905	10.699	15.166	10.849
	2	16.720	22.616	19.061	10.991	16.675	13.286
	3	19.057	31.876	20.371	13.723	23.044	19.209
	4	19.059	33.500	30.428	18.281	25.242	21.078
	5	27.442	35.646	32.256	19.209	30.857	24.761
	6	29.889	38.604	34.503	21.824	31.958	29.332
FG-V	1	10.474	15.961	11.937	9.4116	14.400	9.6145
	2	16.118	22.200	19.060	9.8096	16.060	12.426
	3	19.056	30.880	19.870	12.989	22.683	19.211
	4	19.057	33.271	28.751	18.239	25.212	20.663
	5	27.175	34.871	32.012	19.210	29.780	24.723
	6	28.161	38.596	33.210	21.512	31.019	27.535
FG-O	1	9.6642	15.334	11.192	8.4737	13.707	8.7069
	2	15.557	21.714	19.062	8.9714	15.477	11.761
	3	19.058	30.003	19.364	12.367	22.221	19.211
	4	19.060	32.850	27.303	18.282	25.246	20.184
	5	26.711	34.122	31.584	19.210	28.846	24.765
	6	26.723	37.612	32.048	21.045	30.187	25.996
FG-X	1	12.737	17.204	13.975	11.992	15.794	12.104
	2	17.510	23.086	19.062	12.189	17.220	14.256
	3	19.058	32.740	21.080	14.604	23.493	19.211
	4	19.060	33.917	31.844	18.282	25.246	21.724
	5	28.001	36.391	32.788	19.210	31.774	24.765
	6	31.320	38.612	35.676	22.405	32.782	30.824



**Fig. 9.** Free vibration modal shapes of four edges fully clamped FG-V CNTRC plate. (a) 1st Mode ( $m = 1, n = 1$ ); (b) 2nd Mode ( $m = 1, n = 2$ ); (c) 3rd Mode ( $m = 1, n = 3$ ); (d) 4th Mode ( $m = 1, n = 4$ ); (e) 5th Mode ( $m = 2, n = 1$ ); and (f) 6th Mode ( $m = 2, n = 2$ ).

## 5. Conclusions

CNTs are regarded as promising for application in excellent candidate of the reinforcement of polymer composites such as CNTRC plates, due to their superior mechanical properties, i.e. high strength and stiffness. In this paper, we aim to investigate the free vibration of various types of CNTRC plates using the element-free  $kp$ -Ritz method. The effective material properties of CNTRCs can be estimated by either the Eshelby–Mori–Tanaka approach or the extended rule of mixture. The first-order shear deformation theory is employed to account for the transverse shear effect and rotary inertia and a kernel particle estimate is used to approximate the two-dimensional displacement field. Several numerical examples are provided to verify the accuracy of the present mesh-free method and the results agree well with solutions available in the literature. Detailed parametric studies are conducted to investigate effects of several parameters including CNT volume fraction, plate width-to-thickness ratio, plate aspect ratio, temperature, boundary condition and distribution type of CNTs on natural frequencies and vibration mode shapes of CNTRC plates. Some typical conclusions are given as.

- For CNT volume fraction, it is found that an increase in the CNT volume fraction increases the non-dimensional fundamental frequency of various types of CNTRC plates.
- We also discover that the non-dimensional fundamental frequency of various types of CNTRC plates increase when the plate width-to-thickness ratio increases. It is worth to note that the non-dimensional fundamental natural frequency becomes less sensitive to the change of plate width-to-thickness ratio with the increase of plate width-to-thickness ratio.
- For plate aspect ratio, it can be seen that the non-dimensional fundamental frequency decreases as plate aspect ratio increases for UN-CNTRC plates and the other three types of FG-CNTRC plates.

- For various types of CNTRC plates with different boundary conditions, the highest and lowest values of non-dimensional fundamental natural frequency are occurred for CNTRC plates with CCCC and SFSF boundary conditions, respectively.
- For distribution types of CNTs in the plates, we conclude that reinforcements distributed close to top and bottom are more efficient than those distributed near the mid-plane for increasing the stiffness of CNTRC plates.

## References

- Treacy MMJ, Ebbesen TW, Gibson JM. Exceptionally high Young's modulus observed for individual carbon nanotubes. *Nature* 1996;381:678–80.
- Wong EW, Sheehan PE, Lieber CM. Nanobeam mechanics: elasticity, strength, and toughness of nanorods and nanotubes. *Science* 1997;277:1971–5.
- Salvetat JP, Briggs GAD, Bonard JM, Bacsá RR, Kulik AJ, Stöckli T, et al. Elastic and shear moduli of single-walled carbon nanotube ropes. *Phys Rev Lett* 1999;82:944–7.
- Zhou G, Duan W, Gu B. First-principles study on morphology and mechanical properties of single-walled carbon nanotube. *Chem Phys Lett* 2001;333:344–9.
- Jin L, Bower C, Zhou O. Alignment of carbon nanotubes in a polymer matrix by mechanical stretching. *Appl Phys Lett* 1998;73:1197–9.
- Bower C, Rosen R, Jin L, Han J, Zhou O. Deformation of carbon nanotubes in nanotube–polymer composites. *Appl Phys Lett* 1999;74:3317–9.
- Haggenmueller R, Gommans HH, Rinzler AG, Fischer JE, Winey KI. Aligned single-wall carbon nanotubes composites by melt processing methods. *Chem Phys Lett* 2000;330:219–25.
- Thostenson ET, Chou TW. Processing–structure–multi-functional property relationship in carbon nanotube/epoxy composites. *Carbon* 2006;44:3022–9.
- Thostenson ET, Li C, Chou TW. Nanocomposites in context. *Compos Sci Technol* 2005;65:491–516.
- Lau AKT, Hui D. The revolutionary creation of new advanced materials–carbon nanotube composites. *Compos Part B* 2002;33:263–77.
- Harris PJF. Carbon nanotubes and related structures: new materials for the twenty-first century. Cambridge University; 2001.
- Ajayan PM, Stephan O, Colliex C, Trauth D. Aligned carbon nanotube arrays formed by cutting a polymer resin–nanotube composite. *Science* 1994;265:1212–4.
- Cadek M. Morphological and mechanical properties of carbon–nanotube-reinforced semicrystalline and amorphous polymer composites. *Appl Phys Lett* 2002;81:5123.
- Odegard GM, Gates TS, Wise KE, Park C, Siochi EJ. Constitutive modeling of nanotube–reinforced polymer composites. *Compos Sci Technol* 2003;63:1671–87.
- Griebel M, Hamaekers J. Molecular dynamics simulations of the elastic moduli of polymer–carbon nanotube composites. *Comput Meth Appl Mech Eng* 2004;193:1773–88.
- Fidelus JD, Wiesel E, Gojny FH, Schulte K, Wagner HD. Thermo-mechanical properties of randomly oriented carbon/epoxy nanocomposites. *Compos Part A* 2005;36:1555–61.
- Wuite J, Adali S. Deflection and stress behaviour of nanocomposite reinforced beams using a multiscale analysis. *Compos Struct* 2005;71:388–96.
- Vodenitcharova T, Zhang LC. Bending and local buckling of a nanocomposite beam reinforced by a single-walled carbon nanotube. *Int J Solids Struct* 2006;43:3006–24.
- Formica G, Lacarbonara W, Alessi R. Vibrations of carbon nanotube-reinforced composites. *J Sound Vib* 2010;329:1875–89.
- Arani A, Maghamikia S, Mohammadimehr M, Arefmanesh A. Buckling analysis of laminated composite rectangular plates reinforced by SWCNTs using analytical and finite element methods. *J Mech Sci Technol* 2011;25:809–20.
- Yamanouchi M, Koizumi M, Hirai T, Shiota I. Overall view of the P/M fabrication of functionally gradient materials. In: Proceedings of the first international symposium on functionally gradient materials, 1990. p. 59–64.
- Koizumi M. The concept of FGM, ceramic transactions. *Funct Gradient Mater* 1993;34:3–10.
- Shen HS. Nonlinear bending of functionally graded carbon nanotube-reinforced composite plates in thermal environments. *Compos Struct* 2009;91:9–19.
- Zhu P, Lei ZX, Liew KM. Static and free vibration analyses of carbon nanotube-reinforced composite plates using finite element method with first order shear deformation plate theory. *Compos Struct* 2012;94:1450–60.
- Ke LL, Yang J, Kitipornchai S. Nonlinear free vibration of functionally graded carbon nanotube-reinforced composite beams. *Compos Struct* 2010;92:676–83.
- Shen HS, Zhang CL. Thermal buckling and postbuckling behavior of functionally graded carbon nanotube-reinforced composite plates. *Mater Des* 2010;31:3403–11.
- Lucy LB. Numerical approach to the testing of the fission hypothesis. *Astron J* 1977;82:1013–24.

- [28] Hughes TJR, Cottrell JA, Bazilevs Y. Isogeometric analysis: CAD, finite elements, NURBS, exact geometry and mesh refinement. *Comput Meth Appl Mech Eng* 2005;194:4135–95.
- [29] Nayroles B, Touzot G, Villon P. Generalizing the finite element method: diffuse approximation and diffuse elements. *Comput Mech* 1992;10:307–18.
- [30] Arroyo M, Ortiz M. Local maximum-entropy approximation schemes: a seamless bridge between finite elements and meshfree methods. *Int J Numer Meth Eng* 2006;65:2167–202.
- [31] Cyron CJ, Arroyo M, Ortiz M. Smooth, second order, non-negative meshfree approximants selected by maximum entropy. *Int J Numer Meth Eng* 2009;79:1605–32.
- [32] Li B, Habbal F, Ortiz M. Optimal transportation meshfree approximation schemes for fluid and plastic flows. *Int J Numer Meth Eng* 2010;83:1541–79.
- [33] Fraternali F, Lorenz CD, Marcelli G. On the estimation of the curvatures and bending rigidity of membrane networks via a local maximum-entropy approach. *J Comput Phys* 2012;231:528–40.
- [34] Belytschko T, Lu YY, Gu L. Element-free Galerkin methods. *Int J Numer Meth Eng* 1994;37:229–56.
- [35] Krysl P, Belytschko T. Analysis of thin shells by the element-free Galerkin method. *Int J Solids Struct* 1996;33:3057–80.
- [36] Krysl P, Belytschko T. Analysis of thin plates by the element-free Galerkin method. *Comput Mech* 1995;17:26–35.
- [37] Liew KM, Ren J, Kitipornchai S. Analysis of the pseudoelastic behavior of a SMA beam by the element-free Galerkin method. *Eng Anal Bound Elem* 2004;28:497–507.
- [38] Liew K, Peng L, Kitipornchai S. Buckling analysis of corrugated plates using a mesh-free Galerkin method based on the first-order shear deformation theory. *Comput Mech* 2006;38:61–75.
- [39] Peng L, Kitipornchai S, Liew K. Free vibration analysis of folded plate structures by the FSDT mesh-free method. *Comput Mech* 2007;39:799–814.
- [40] Zhu P, Liew KM. Free vibration analysis of moderately thick functionally graded plates by local Kriging meshless method. *Compos Struct* 2011;93:2925–44.
- [41] Liew KM, Wang J, Ng TY, Tan MJ. Free vibration and buckling analyses of shear-deformable plates based on FSDT meshfree method. *J Sound Vib* 2004;276:997–1017.
- [42] Atluri SN, Zhu T. A new Meshless Local Petrov–Galerkin (MLPG) approach in computational mechanics. *Comput Mech* 1998;22:117–27.
- [43] Chen JS, Pan C, Wu CT, Liu WK. Reproducing Kernel Particle methods for large deformation analysis of non-linear structures. *Comput Meth Appl Mech Eng* 1996;139:195–227.
- [44] Zhao X, Li Q, Liew KM, Ng TY. The element-free-Ritz method for free vibration analysis of conical shell panels. *J Sound Vib* 2006;295:906–22.
- [45] Liew KM, Wang J, Tan MJ, Rajendran S. Postbuckling analysis of laminated composite plates using the mesh-free *kp*-Ritz method. *Comput Meth Appl Mech Eng* 2006;195:551–70.
- [46] Zhao X, Liew KM, Ng TY. Vibration analysis of laminated composite cylindrical panels via a meshfree approach. *Int J Solids Struct* 2003;40:161–80.
- [47] Liew KM, Ng TY, Zhao X, Reddy JN. Harmonic reproducing kernel particle method for free vibration analysis of rotating cylindrical shells. *Comput Meth Appl Mech Eng* 2002;191:4141–57.
- [48] Sobhani Aragh B, Nasrollah Barati AH, Hedayati H. Eshelby–Mori–Tanaka approach for vibrational behavior of continuously graded carbon nanotube-reinforced cylindrical panels. *Compos Part B* 2012;43:1943–54.
- [49] Wang J, Pyrz R. Prediction of the overall moduli of layered silicate-reinforced nanocomposites – Part I: Basic theory and formulas. *Compos Sci Technol* 2004;64:925–34.
- [50] Shen HS. Postbuckling of nanotube-reinforced composite cylindrical shells in thermal environments, Part I: Axially-loaded shells. *Compos Struct* 2011;93:2096–108.
- [51] Giordano S, Palla PL, Colombo L. Nonlinear elasticity of composite materials. *Eur Phys J B* 2009;68:89–101.
- [52] Eshelby JD. The determination of the elastic field of an ellipsoidal inclusion, and related problems. *Proc Roy Soc Lond, Ser A* 1957;241:376–96.
- [53] Mori T, Tanaka K. Average stress in matrix and average elastic energy of materials with misfitting inclusions. *Acta Metall* 1973;21:571–4.
- [54] Benveniste Y. A new approach to the application of Mori–Tanaka’s theory in composite materials. *Mech Mater* 1987;6:147–57.
- [55] Mura T. *Micromechanics of defects in solids*. 2nd ed. The Netherlands: Martinus Nijhoff; 1987.
- [56] Reddy JN. *Mechanics of laminated composite plates and shells: theory and analysis*. 2nd ed. Boca Raton (FL): CRC Press; 2004.
- [57] Efraim E, Eisenberger M. Exact vibration analysis of variable thickness thick annular isotropic and FGM plates. *J Sound Vib* 2007;299:720–38.
- [58] Liu WK, Jun S, Zhang YF. Reproducing kernel particle methods. *Int J Numer Meth FL* 1995;20:1081–106.
- [59] Han Y, Elliott J. Molecular dynamics simulations of the elastic properties of polymer/carbon nanotube composites. *Comput Mater Sci* 2007;39:315–23.
- [60] Chang TC, Geng JY, Guo XM. Chirality- and size-dependent elastic properties of single-walled carbon nanotubes. *Appl Phys Lett* 2005;87.
- [61] Elliott JA, Sandler JKW, Windle AH, Young RJ, Shaffer MSP. Collapse of single-wall carbon nanotubes is diameter dependent. *Phys Rev Lett* 2004;92:095501.
- [62] Jin Y, Yuan FG. Simulation of elastic properties of single-walled carbon nanotubes. *Compos Sci Technol* 2003;63:1507–15.
- [63] Liew KM, Yan JW, Sun YZ, He LH. Investigation of temperature effect on the mechanical properties of single-walled carbon nanotubes. *Compos Struct* 2011;93:2208–12.
- [64] Wang CY, Zhang LC. A critical assessment of the elastic properties and effective wall thickness of single-walled carbon nanotubes. *Nanotechnology* 2008;19:075075.
- [65] Wang ZX, Shen HS. Nonlinear vibration of nanotube-reinforced composite plates in thermal environments. *Comput Mater Sci* 2011;50:2319–30.